CHEMISTRY OF MATERIALS

pubs.acs.org/cm

Article

Quantifying Dynamic Tilting in Halide Perovskites: Chemical Trends and Local Correlations

Julia Wiktor,* Erik Fransson, Dominik Kubicki, and Paul Erhart*

Cite This: *Chem. Mater.* 2023, 35, 6737−6744

Read Online

ACCESS | Metrics & More | Article Recommendations | Supporting Information

ABSTRACT: Halide perovskites have emerged as one of the most interesting materials for optoelectronic applications due to their favorable properties, such as defect tolerance and long charge carrier lifetimes, which are attributed to their dynamic softness. However, this softness has led to apparent disagreements between the local instantaneous and global average structures of these materials. In this study, we rationalize this situation through an assessment of the local tilt angles of octahedra in the perovskite structure using large-scale molecular dynamics simulations based on machine-learned potentials trained using density functional theory calculations. We compare structural properties given by different density functionals [local density approximation, PBE, PBE + D3, PBEsol, strongly constrained and appropriately normed (SCAN), SCAN + rVV10, and van der Waals density functional with consistent exchange] and establish trends across a family of $CsMX_3$ perovskites with M = Sn or Pb and X = Cl, Br or I. Notably, we demonstrate strong short-range ordering in the cubic phase of halide perovskites. This ordering is reminiscent of the tetragonal phase and provides the bridge between the disordered local structure and the global cubic arrangement. Our results provide a deeper understanding of the structural properties of halide perovskites and their local distortions, which is crucial for further understanding their optoelectronic properties.

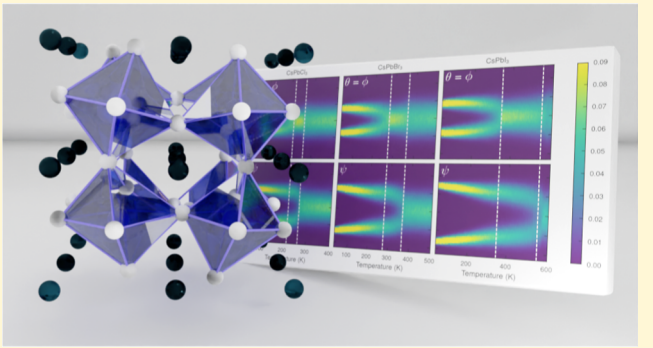

INTRODUCTION

Halide perovskites have gained significant attention as promising materials for various applications, including high-efficiency solar cells,[1−3] lasers,[4] light-emitting diodes,[5] and more.[6] Their exceptional performance is attributed to various factors, such as defect tolerance[7−9] and long carrier lifetimes.[10−13] These properties are linked to the high dielectric constants of these materials and effective screening of charges,[14,15] which in turn can be traced back to their dynamic softness and ability to dynamically respond to the presence of excess charges. Despite their importance, understanding and quantifying the underlying dynamics of halide perovskites remain challenging.

Several previous studies have highlighted the crucial role played by the dynamic local structure and octahedral tilting in halide perovskites.[16] For example, some investigations have revealed that ignoring the local structure can lead to inaccurate interpretation of various experimental techniques, including X-ray absorption near edge structure spectroscopy,[17] high-energy resolution inelastic X-ray scattering,[18] and pair distribution function analysis.[19−21] Moreover, electronic structure calculations performed for simulation cells corresponding to the average perovskite structure have been shown to result in poor estimates of band gaps,[21−24] emphasizing that it is critical to account for transient local distortions. These findings underscore the importance of understanding the dynamic nature of halide perovskites and its implications for a wide range of applications.

Octahedral tilting, being one of the key properties of halide perovskites, has been assessed in several previous computational studies. One of the simplest indicators of how much materials will distort at finite temperatures can already be extracted from static calculations of potential energy surfaces or phonon dispersion curves at 0 K, as has been done for instance in refs 25 and 26. While this allows one to also compare the performance of various exchange−correlation functionals,[27] it is not possible to predict the exact dynamic properties of a material from calculations done at 0 K alone. Therefore, molecular dynamics (MD) simulations have been used to study the dynamics of halide perovskites more directly, for instance to contrast different functionals,[28,29] to verify the effect of cation mixing[30] or to understand the local disorder and its effect on experimental observations.[17,31] Various dynamic properties have been used in these studies to quantify

Received: April 19, 2023
Revised: August 7, 2023
Published: August 21, 2023

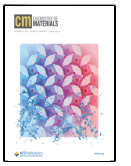

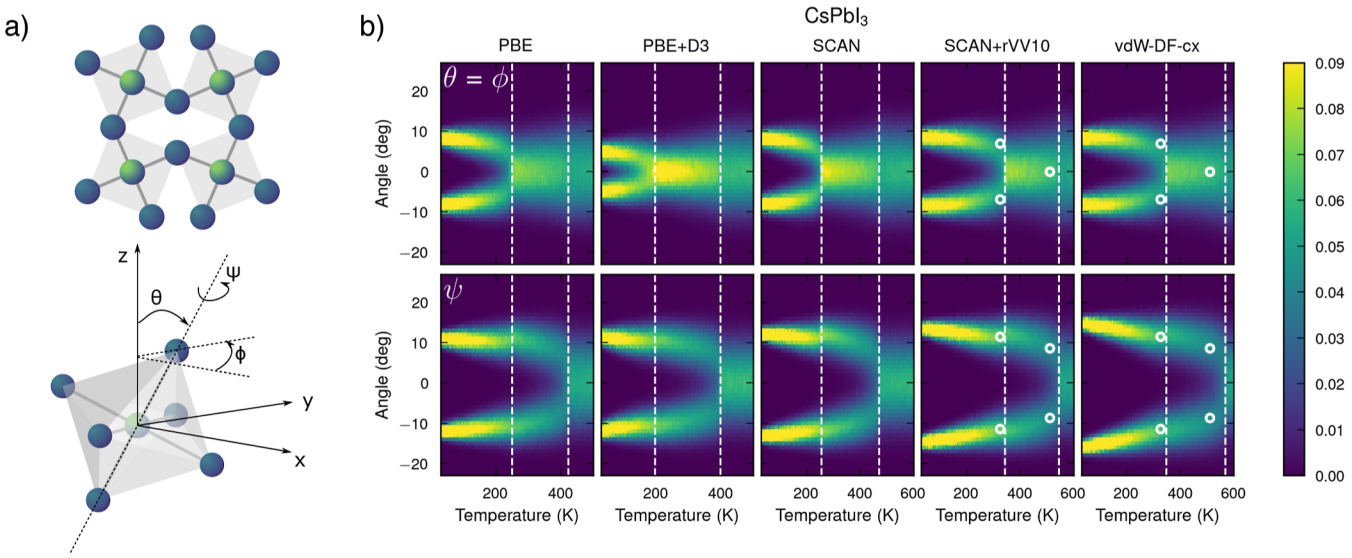

Figure 1. (a) Representation of the $CsPbI_3$ perovskite structure with PbI_6 octahedra indicating the definition of the three Euler angles θ, ϕ, and ψ, describing the orientation of the octahedron. (b) Maps of tilt angles as a function of temperature in PBE, PBE + D3, SCAN, SCAN + rVV10, and vdW-DF-cx functionals. Dashed vertical lines indicate the orthorhombic-to-tetragonal and tetragonal-to-cubic phase transitions. For the best-performing SCAN + rVV10 and vdW-DF-cx functionals, we mark (with white circles) the angles determined from experimental structures reported in ref 53.

the disorder, such as the evolution of a single M−X−M angle,[30] distributions of M−X−M tilt angles[17,32] or distributions of halogen displacements.[28,32]

In this work, we quantify the local octahedral tilting of halide perovskites through large-scale MD simulations and assess trends across functionals, temperatures, and material chemistries. We use neuroevolution potential (NEP) models to accelerate MD simulations based on density functional theory (DFT) calculations. In the case of α-$CsPbI_3$, we find that different functionals lead to similar trends in tilt angle distributions within the same phase, but very different phase transition temperatures. Focusing further on the van der Waals density functional with consistent exchange (vdW-DF-cx) functional, we assess the trends across the $CsMX_3$ family of inorganic perovskites with varying halogen atoms (X = Cl, Br, and I) and metal cation (M = Sn and Pb). We finally create a bridge between the local environment of a single octahedron and the global perovskite structure by assessing the correlation between neighboring units.

METHODS

Machine-Learned Potential Construction. We constructed third-generation (NEP3) NEP models[33,34] using a boot-strapping strategy, as described in detail in ref 29. In this process, we included the cubic ($Pm\bar{3}m$), two tetragonal ($I4/mcm$, and $P4/mbm$), and one orthorhombic ($Pnma$) structure, as well as the so-called delta-phase ($Pnma$). The model construction was carried out using the GPUMD package[34] as well as the CALORINE package[35] and HIPHIVE packages[36] for data preparation and analysis. The performance of the final models is summarized in Table S1 of the Supporting Information.

DFT Calculations. To generate input data for model construction, we performed DFT calculations using the projector augmented-wave method (PAW) method[37,38] as implemented in the Vienna Ab-initio Simulation package.[39,40] Our calculations use a Γ-centered $\boldsymbol{k}$-point grid with a spacing of 0.18 $Å^{-1}$ and a Gaussian smearing width of 0.1 eV. Seven different exchange−correlation functionals were used, namely the local density approximation (LDA), PBE,[41] PBE + D3, PBESol,[42] the strongly constrained and appropriately normed (SCAN) functional,[43] SCAN + rVV10,[44] and the vdW-DF-cx method.[45,46] The valence electron configurations used in the PAW data sets are provided in Table S2 in the Supporting Information. We used a plane-wave energy cutoff of 520 eV for all materials.

MD Simulations. MD simulations were carried out using the GPUMD package.[34,47] During the simulations, the temperature was continuously increased from 20 to up to 620 K over a period of 100 ns, yielding a heating rate of 6 K ns^{-1}. For some compounds with low transition temperatures, we terminated the simulations already at 420 or 520 K. The simulations were run in the NpT ensemble, with temperature and pressure controlled using stochastic velocity[48] and cell rescaling.[49] The time step is set to 5 ps, and the pressure to zero. The simulation cell comprised 16 × 16 × 12 repetitions of the primitive unit cell of the orthorhombic perovskite structure, corresponding to 61 440 atoms.

Analysis of Tilt Angles. The tilt angles were extracted using the following procedure, which has been implemented using functionality from OVITO:[50] First the bonds between the M cations and X anions are generated, which yields six bonds per M atom. Next, each MX_6 octahedron is matched to a simple cubic environment, i.e., an undistorted fully symmetric octahedron as it would occur in the ideal cubic perovskite structure, using the algorithm described in Larsen et al.[51] This yields the scaling and rotation needed to achieve optimal mapping. The rotation is represented in OVITO in quaternion form, which is then cast to Euler angles using functionality from the SCIPY package.[52] Among the three possible settings for the internal rotations, we select the one that yields the angles in increasing magnitude, following the principle established by Glazer. This analysis was carried out for each snapshot of the heating (and cooling) runs, giving us access to the angle distribution as a practically continuous function of temperature.

RESULTS

Comparison of Functionals. We first compare the distributions of octahedral tilt angles computed for $CsPbI_3$ according to NEP models representing five different functionals: the widely used PBE functional,[41] its version including dispersion corrections PBE + D3, the SCAN functional,[43] which has shown good performance for halide perovskites in comparison with calculations based on the random phase approximation,[54] its version including additional dispersion corrections SCAN + rVV10, and the vdW-DF-cx method.[45,46]

https://doi.org/10.1021/acs.chemmater.3c00933
Chem. Mater. 2023, 35, 6737−6744

To simplify the comparison, here, we omit the results for the LDA and PBEsol functionals,[42] which can, however, be found in Figure S1 of the Supporting Information. The distributions for all temperatures are shown in Figure 1 as maps of tilt angles. The transition temperatures from the orthorhombic (*Pnma*) to the tetragonal (*P*4/*mbm*) phase at lower temperatures and from the tetragonal to the cubic $Pm\bar{3}m$ phase at higher temperatures as obtained from the evolution of the lattice parameters are indicated by vertical dashed lines. Phase transition temperatures based on the models for all seven functionals are given in Table 1 and compared to experimental values.

Table 1. Phase Transition Temperatures in K Found Using Different Functionals for $CsPbI_3$[a]

	ortho.−tetra	tetra.−cubic
LDA	372	546
PBE	250	423
PBE + D3	197	399
PBEsol	269	445
SCAN	256	472
SCAN + rVV10	344	544
vdW-DF-cx	348	569
experiment	457	554

[a]Values were extracted from the temperature dependence of the heat capacity.[29] Experimental values are given for comparison.[53]

At low temperatures, the angle splitting is similar for all models (functionals), except for the PBE + D3 method, which clearly underestimates this property. The $\theta = \phi$ angle, characterizing the tilt in the z direction in the orthorhombic structure has a magnitude of just below 10° in most cases. The ψ angle, related to the octahedral rotation in the $x - y$ plane, is slightly larger than 10°. The temperature evolution of the angles is also qualitatively similar, with the main difference being related to phase transition temperatures (see Table 1), with SCAN + rVV10 and vdW-DF-cx giving the highest transition temperatures (the closest to experimental values) and PBE + D3 giving the lowest.[29] We note that the LDA functional also gives transition temperatures close to experiment; however, we consider this mostly to be a result of error cancellation. For the two best-performing functionals, SCAN + rVV10 and vdW-DF-cx, we also compare the tilt angles with their experimental counterparts determined in ref 53. Measurements indicate average angles of $\theta = \phi = \pm 6.9°$, and $\psi = \pm 11.5°$ in the orthorhombic structure at 345 K. In the tetragonal structure at 510 K, $\theta = \phi$ amounts to 0°, and ψ to ±8.6°. These values are close to the maxima of the tilt angle distributions at the corresponding temperatures for both functionals. It is worth noting that while experimentally determined structures correspond to the average geometry, our results clearly show that there is a relatively broad distribution of instantaneous tilting angles in all phases. This has been previously pointed out for example for the cubic structure of $CsPbBr_3$.[17]

To enable a more straightforward comparison of angular distributions between the models representing different functionals, we now analyze tilting at three selected temperatures, 150, 300, and 500 K (Figure 2).

At 150 K, all models (functionals) correctly predict $CsPbI_3$ to exhibit the orthorhombic structure. While the $\theta = \phi$ distributions are almost identical for all functionals with the exception of PBE + D3, the separation of the maxima in the ψ distribution clearly increases in the order PBE + D3, PBE, SCAN, SCAN + rVV10, vdW-DF-cx.

Next, we focus on the temperature of 300 K, corresponding to the most common value used in MD simulations for halide perovskites. At this temperature, $CsPbI_3$ should exhibit the orthorhombic structure, according to experiments.[53] Strikingly, among the considered functionals, only the SCAN + rVV10 and vdW-DF-cx-based models predict this phase to be stable at 300 K, which is reflected in angle splitting for all three Euler angles. With the PBE, PBE + D3, and SCAN-based models we observe $\theta = \phi$ distributions of similar broadening with one maximum only, indicating the tetragonal phase. For ψ, all functionals yield a bimodal distribution. The splitting of the maxima is larger for the SCAN, SCAN + rVV10, and vdW-DF-cx-based models and smaller for PBE, and PBE + D3. The differences between the distributions of $\theta = \phi$ achieved with

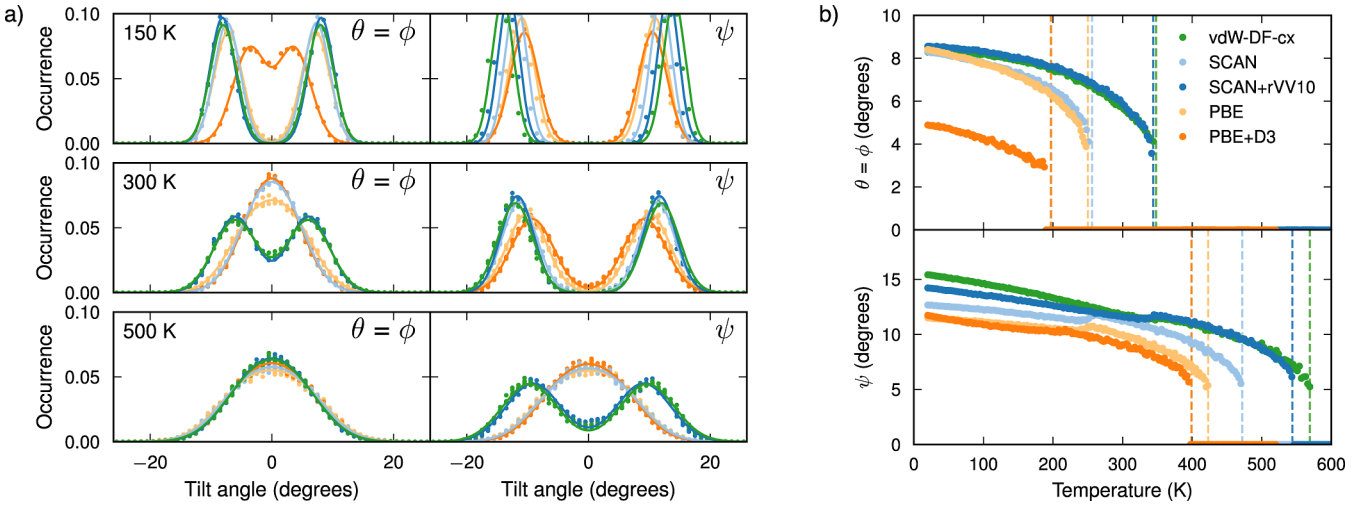

Figure 2. (a) Probability distribution of octahedral tilts in $CsPbI_3$ as described by the three Euler angles θ, ϕ, and ψ. Data obtained with NEP models based on five different functionals (vdW-DF-cx, SCAN, SCAN + rVV10, PBE, and PBE + D3) are shown at three different temperatures. Solid lines are double Gaussian fits to the data. (b) Position of the maximum in the tilt angle distribution as extracted from double Gaussian fits. Vertical dashed lines indicate phase transitions.

https://doi.org/10.1021/acs.chemmater.3c00933
Chem. Mater. 2023, 35, 6737−6744

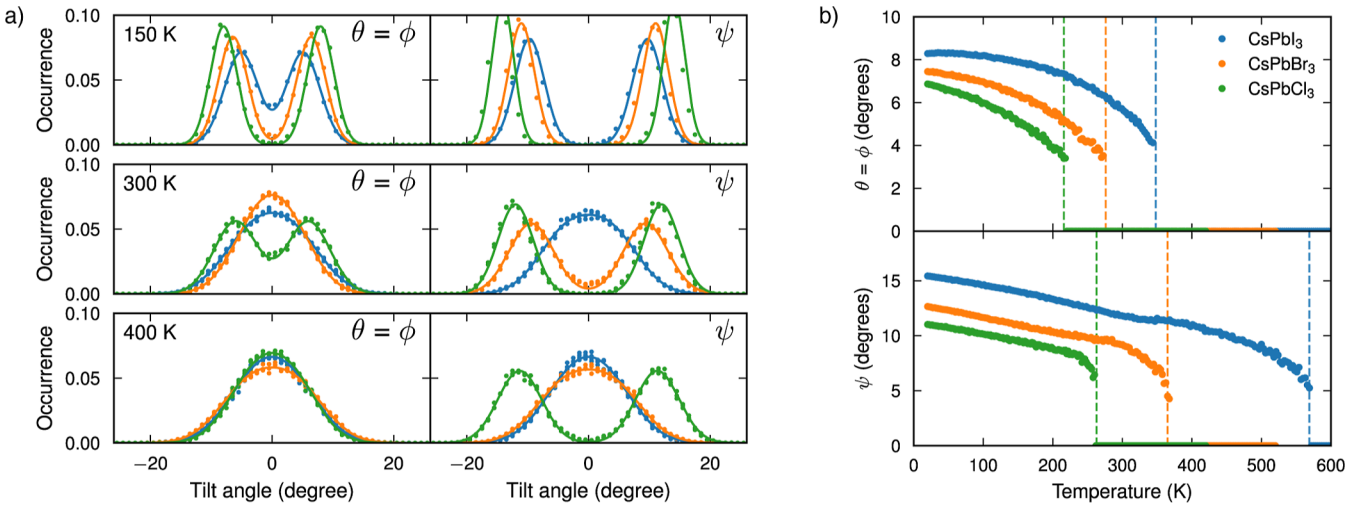

Figure 3. (a) Probability distribution of octahedral tilts at 150, 300, and 400 K in $CsPbCl_3$, $CsPbBr_3$, and $CsPbI_3$, as described by the three Euler angles θ, ϕ, and ψ. (b) Position of the maximum in the tilt angle distribution as extracted from double Gaussian fits. Vertical dashed lines indicate phase transitions.

different functionals highlight the importance of choosing the right computational setting for constant-temperature MD simulations. We thus expect that room-temperature simulations of $CsPbI_3$ in the orthorhombic phase using, e.g., PBE, PBE + D3 or SCAN could lead to spurious distortions in the cell due to the drive towards the tetragonal phase.

At 500 K, only SCAN + rVV10, and vdW-DF-cx correctly predict the tetragonal phase with very similar angle distributions. PBE, PBE + D3, and SCAN predict the cubic phase, with broad Gaussian distributions centered around 0° for all angles.

We note that a broad distribution of octahedral tilting angles is the reason for a large difference in the local and global symmetry in halide perovskites.[17,22] While on average the structure at high temperatures exhibits a high-symmetry tetragonal or cubic structure, locally each octahedron is likely to be significantly tilted, with a standard deviation (see Figure S6 in the Supporting Information) from the average position of up to 7° in each direction. The difference between the average and instantaneous structure can affect the electronic structure calculation and interpretation of experimental measurements. For example, calculations performed using high-symmetry cubic cells have been shown to underestimate band gaps of inorganic perovskites by up to 0.8 eV.[22] Also, in $CsPbBr_3$ it has been shown that calculations based on the average experimental structure were not sufficient to explain the measured X-ray absorption near edge structure spectra and dynamic disorder needed to be taken into account.[17] This is due to the fact that the electron-phonon coupling is significant and electronic structure depends strongly on the local environment, which is not captured by the averaged structure models.

To further analyze the data, we fit the angle distributions with a symmetric double Gaussian function of the form

$$p(x) = \frac{1}{2\sigma\sqrt{2\pi}}\left(e^{-1/2(x-\mu)^2/\sigma^2} + e^{-1/2(x+\mu)^2/\sigma^2}\right)$$

where μ and σ are the mean and standard deviation, respectively. The fitting is done with a small regularization for the free parameters μ and σ to reduce noise when fitting the distributions from the cubic phase.

The positions of the maxima of the distributions (μ) as a function of temperature are plotted in Figure 2b. The figure indicates that the splitting of the tilt angles exhibits a similar temperature dependence for all models (functionals). The rate at which the position of the maxima changes depends, however, on the particular functional. We also note that a rapid change in the positions of the maxima of the distributions agrees very well with phase transition temperatures (indicated by dashed lines in the figure) extracted from the lattice parameters. Moreover, we notice a correlation between the magnitude of the splitting in the angular distribution at low temperatures and the transition temperatures, with higher splittings corresponding to higher transition temperatures. This, e.g., underpins why the PBE + D3 method leads to a very poor agreement with experiments, as it predicts low splitting in the $\theta = \phi$ angle at low temperatures.

Chemical Trends. We now focus on the vdW-DF-cx functional and compare different compounds. We note that the performance of the SCAN + rVV10 method is very similar, and the choice of this functional would most likely lead to the same conclusions below. We first analyze the effect of varying the halogen atom within the family of compounds $CsPbX_3$ with X = Cl, Br, and I. Tilting angle maps as well as transition temperatures can be found in the SM, while in Figure 3 we show the distributions at three temperatures (150, 300, and 400 K) as well as the positions of maxima in the angular distributions. At low temperatures, all three materials exhibit the orthorhombic *Pnma* phase consistent with bimodal distributions of all three Euler angles. The splitting between the maxima of both the $\theta = \phi$ and ψ angles increases with the size of the halogen ion, following the sequence Cl−Br−I trend. As can be seen in Figure 3b, this ordering is retained at all temperatures.

At 300 K, $CsPbCl_3$ undergoes a phase transition from the tetragonal to the cubic phase, which explains the mixed nature of the ψ angle distribution. $CsPbBr_3$ is stable in the tetragonal phase, with a unimodal distribution of $\theta = \phi$ and a bimodal distribution of ψ. $CsPbI_3$ is still orthorhombic at 300 K and exhibits the bimodal distribution of all Euler angles. We note that for $CsPbCl_3$, 300 K is exactly the phase transition temperature according to the vdW-DF-cx-based model, which

https://doi.org/10.1021/acs.chemmater.3c00933
Chem. Mater. 2023, 35, 6737−6744

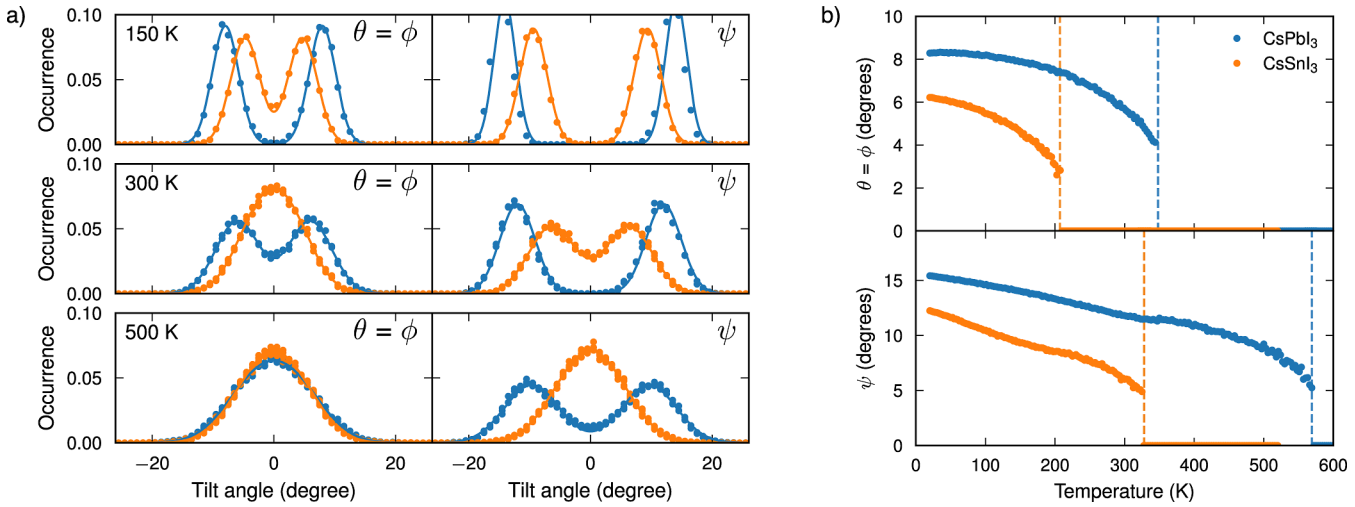

Figure 4. (a) Probability distribution of octahedral tilts 150, 300, and 500 K in $CsSnI_3$ and $CsPbI_3$ compounds, as described by the three Euler angles θ, ϕ, and ψ. (b) Position of the maximum in the tilt angle distribution as extracted from double Gaussian fits. Vertical dashed lines indicate phase transitions.

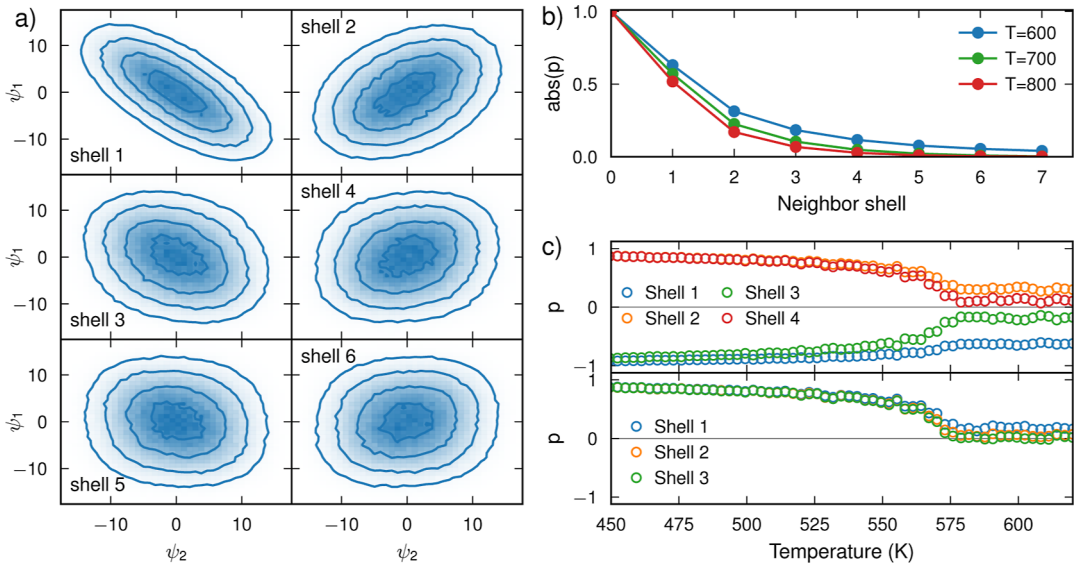

Figure 5. (a) Joint probability distribution $P(\psi_1, \psi_n)$ for tilt angles between octahedra in different neighbor shells along the [100] direction at 600 K for $CsPbI_3$. (b) Absolute cCorrelation $|p|$ as a function of the neighbor shell for 600, 700, and 800 K along the [100] direction. (c) Correlation p as a function of temperature along the [100] (top) and [001] (bottom) directions, where [001] is the rotation axis for ψ. Here, data in (a,b) are from constant temperature MD runs in cubic supercells consisting of 69 120 atoms, whereas data in (c) comes from a heating run.

explains the mixed tetragonal/cubic distribution of the ψ tilting angle. At 400 K, $CsPbI_3$ is tetragonal, while both $CsPbBr_3$ and $CsPbCl_3$ are cubic. This allows for a direct comparison between the latter two. While the plots in Figure 3a are rather similar, the distribution for $CsPbCl_3$ is slightly more narrow, suggesting that the octahedral tilting is reduced for smaller halogen ions.

We now evaluate the effect of the metal cation, by making a comparison between $CsPbI_3$ and $CsSnI_3$ (Figure 4). At 150 K, both $CsPbI_3$ and $CsSnI_3$ adopt the orthorhombic phase. The tilt angle splitting is much more pronounced in $CsPbI_3$ than in $CsSnBr_3$. The smaller magnitude of tilt angles at low temperatures for $CsSnI_3$ is correlated with much lower phase transition temperatures as compared to $CsPbI_3$ (see Table S3 in the Supporting Information).

Local Tilt Angle Correlations. From analyzing the tilt angle distributions, it is clear that at high temperatures halide perovskites are cubic on a global scale corresponding to $\mu = 0$. However, locally each octahedron can still be significantly tilted, with tilt angles reaching the values seen in the tetragonal and orthorhombic phases. In the tetragonal and orthorhombic phases, long-range ordering occurs with respect to the octahedral tilt angles. While in the cubic phase, there is no long-range order, this does not imply the absence of short-range order (correlation) between neighboring octahedra. In the context of local regions in the cubic phase appearing tetragonal or orthorhombic,[17] it is thus of interest to analyze and quantify the short-range order, i.e., assess the correlation between tilt angles of neighboring octahedra, in the cubic phase. Strikingly, a recent study by Doherty et al. found that phases that in X-ray diffraction appear to be cubic, locally feature regions that are tetragonal or orthorhombic.[55] Here, we investigate the joint distribution of the tilt angle of neighboring octahedra, $P(\psi_1, \psi_n)$, where n refers to the n-th neighbor shell

https://doi.org/10.1021/acs.chemmater.3c00933
Chem. Mater. 2023, 35, 6737−6744

in the [100] direction (perpendicular to the rotational axis of ψ) and ψ the tilt-angle around the z-axis (Figure 5a). Note that the same correlation occurs for the symmetrically equivalent [010] direction. The correlation in other directions in the [100]−[010] plane behaves in a very similar way to the [100] direction (Figure S9 in the Supporting Information) and thus for the sake of simplicity we limit the analysis below to the [100] direction. This analysis is carried out for $CsPbI_3$, but the behavior is qualitatively the same for all materials considered here (Figure S7 in the Supporting Information). There is a clear correlation between ψ_1 and ψ_n for small n, which can be quantified with the Pearson correlation p_n defined as

$$p_n = \frac{\langle \psi_1 \psi_n \rangle}{\langle \psi_1 \psi_1 \rangle}$$

The correlation naturally occurs due to the nearest neighbor octahedra sharing one halogen ion (X = I, Br, Cl) atom (Figure 1a). If a given octahedron rotates in one direction its neighbors will thus favorably rotate in the opposite direction. This leads to the sign of the correlation alternating between odd and even neighbor shells along the [100] direction.

The absolute value of the correlation $|p_n|$ decays exponentially with a typical length-scale of about 3 to 5 shells (corresponding to about 20 Å) with the number of the neighbor shell (Figure 5b). We note that at 600 K (and thus above the tetragonal-to-cubic transition temperature), there is a significant correlation between octahedra lying multiple shells apart, stretching as far as the seventh neighbor shell. Although the correlation weakens at temperatures between 600 and 700 K, which is far into the cubic stability region, the orientation of a specific octahedron still has a notable effect on its second and third neighbors.

The full temperature dependence of the correlation p_n (Figure 5c) shows that the correlation increases as the temperature decreases towards the transition to the tetragonal phase. While the tilt angle around the z-axis (ψ) correlates strongly between neighboring octahedra along the [100] direction, there is almost no correlation in the cubic phase between neighboring octahedra along the [001] direction.[a] This is likely due to the fact that the shared X anion for these neighbors does not move when rotating around the z-axis, and thus the octahedra can rotate around the z-axis more independently of each other. In the tetragonal phase, the correlation between all neighboring shells approaches the respective limiting values of ±1, indicating that long-ranged ordering is obtained.

The strong short-range ordering observed in the cubic phase may have implication for the refinement of experimental diffraction data. Since some of the tetragonal ordering is still present in the cubic phase, structure determination can be difficult in these materials. Specifically, our findings put into question the frequently adopted approach of modeling thermal displacement parameters through Debye-Waller factors in this class of materials. The latter (as commonly used) incorporates namely the assumption that the local energy landscape can be approximated as harmonic. Halide perovskites, however, exhibit extreme anharmonicity,[32,53] in particular for the zone boundary modes that are connected to the octahedral tilting.[31] We also note that similar observations of short-range correlations in halide perovskites have been made experimentally for $CsPbBr_3$ by Lanigan-Atkins et al.[56] and for $CH_3NH_3PbI_3$ and $CH_3NH_3PbBr_3$ by Weadock et al.,[57] as well as computationally for $CsPbI_3$ by Baldwin et al.[58]

CONCLUSIONS

In conclusion, in this study, we have explored the local structural properties of inorganic halide perovskites through large-scale MD simulations using machine-learned potentials based on DFT calculations. By assessing the phase transitions and local tilt angles of octahedra in the perovskite structure, we first analyzed the performance of different functionals as described by NEP models, including LDA, PBE, PBE + D3, PBEsol, SCAN, SCAN + rVV10, and vdW-DF-cx. We find that while most models (functionals) underestimate the phase transition temperatures, SCAN + rVV10, and vdW-DF-cx-based models yield values close to the experiment. Focusing subsequently on the vdW-DF-cx method, we then established trends across a family of $CsMX_3$ perovskites. Finally, we demonstrated the presence of strong short-range ordering, reminiscent of the tetragonal phase, even in the cubic phase of halide perovskites above the cubic-to-tetragonal transition temperature. This ordering connects the transiently strongly distorted local structure to the global cubic arrangement and sheds light on the complex interplay between local and global structural properties in these materials. This study provides direct insight into the local disorder in inorganic halide perovskites across a wide temperature range and contributes to a more complete understanding of their structural properties.

ASSOCIATED CONTENT

Supporting Information

The Supporting Information is available free of charge at https://pubs.acs.org/doi/10.1021/acs.chemmater.3c00933.

Maps of tilt angles for all considered functionals and materials, standard deviations of the tilt angle distributions, additional plots of tilt-angle correlations, an overview of NEP models, details of the PAW data sets, and transition temperatures for all compounds (PDF)

AUTHOR INFORMATION

Corresponding Authors

Julia Wiktor − *Department of Physics, Chalmers University of Technology, SE-412 96 Gothenburg, Sweden;* orcid.org/0000-0003-3395-1104; Email: julia.wiktor@chalmers.se

Paul Erhart − *Department of Physics, Chalmers University of Technology, SE-412 96 Gothenburg, Sweden;* orcid.org/0000-0002-2516-6061; Email: erhart@chalmers.se

Authors

Erik Fransson − *Department of Physics, Chalmers University of Technology, SE-412 96 Gothenburg, Sweden;* orcid.org/0000-0001-5262-3339

Dominik Kubicki − *School of Chemistry, University of Birmingham, B15 2TT Birmingham, U.K.;* orcid.org/0000-0002-9231-6779

Complete contact information is available at: https://pubs.acs.org/10.1021/acs.chemmater.3c00933

Notes

The authors declare no competing financial interest.

https://doi.org/10.1021/acs.chemmater.3c00933
Chem. Mater. 2023, 35, 6737−6744

■ ACKNOWLEDGMENTS

This work was funded by the Swedish Research Council (grant numbers 2018-06482, 2019-03993, 2020-04935, 2021-05072), the Area of Advance Nano at Chalmers, and the Chalmers Initiative for Advancement of Neutron and Synchrotron Techniques. J.W. acknowledges the Swedish Strategic Research Foundation through a Future Research Leader programme (FFL21-0129). The computations were enabled by resources provided by the National Academic Infrastructure for Supercomputing in Sweden (NAISS) and the Swedish National Infrastructure for Computing (SNIC) at C3SE, NSC, HPC2N, and PDC partially funded by the Swedish Research Council through grant agreements no. 2022-06725 and no. 2018-05973.

■ ADDITIONAL NOTE

[a]For neighbor shells along the [001] direction, the correlation is always positive due to the in-phase tilting of the $a^0a^0c^+$ phase.

■ REFERENCES

(1) Kojima, A.; Teshima, K.; Shirai, Y.; Miyasaka, T. Organometal Halide Perovskites As Visible-Light Sensitizers for Photovoltaic Cells. *J. Am. Chem. Soc.* **2009**, *131*, 6050−6051.

(2) Kim, H.-S.; Lee, C.-R.; Im, J.-H.; Lee, K.-B.; Moehl, T.; Marchioro, A.; Moon, S.-J.; Humphry-Baker, R.; Yum, J.-H.; Moser, J. E.; et al. Lead Iodide Perovskite Sensitized All-Solid-State Submicron Thin Film Mesoscopic Solar Cell with Efficiency Exceeding 9. *Sci. Rep.* **2012**, *2*, 591.

(3) Hodes, G. Perovskite-Based Solar Cells. *Science* **2013**, *342*, 317−318.

(4) Lei, L.; Dong, Q.; Gundogdu, K.; So, F. Metal Halide Perovskites for Laser Applications. *Adv. Funct. Mater.* **2021**, *31*, 2010144.

(5) Van Le, Q.; Jang, H. W.; Kim, S. Y. Recent Advances Toward High-Efficiency Halide Perovskite Light-Emitting Diodes: Review and Perspective. *Small Methods* **2018**, *2*, 1700419.

(6) Kim, H.; Han, J. S.; Choi, J.; Kim, S. Y.; Jang, H. W. Halide Perovskites for Applications Beyond Photovoltaics. *Small Methods* **2018**, *2*, 1700310.

(7) Kang, J.; Wang, L.-W. High Defect Tolerance in Lead Halide Perovskite $CsPbBr_3$. *J. Phys. Chem. Lett.* **2017**, *8*, 489−493.

(8) Chen, B.; Rudd, P. N.; Yang, S.; Yuan, Y.; Huang, J. Imperfections and Their Passivation in Halide Perovskite Solar Cells. *Chem. Soc. Rev.* **2019**, *48*, 3842−3867.

(9) Kim, G.-W.; Petrozza, A. Defect Tolerance and Intolerance in Metal-Halide Perovskites. *Adv. Energy Mater.* **2020**, *10*, 2001959.

(10) Ponseca, C. S., Jr; Savenije, T. J.; Abdellah, M.; Zheng, K.; Yartsev, A.; Pascher, T.; Harlang, T.; Chabera, P.; Pullerits, T.; Stepanov, A.; et al. Organometal Halide Perovskite Solar Cell Materials Rationalized: Ultrafast Charge Generation, High and Microsecond-Long Balanced Mobilities, and Slow Recombination. *J. Am. Chem. Soc.* **2014**, *136*, 5189−5192.

(11) Edri, E.; Kirmayer, S.; Mukhopadhyay, S.; Gartsman, K.; Hodes, G.; Cahen, D. Elucidating the Charge Carrier Separation and Working Mechanism of $CH_3NH_3PbI_{3-x}Cl_x$ Perovskite Solar Cells. *Nat. Commun.* **2014**, *5*, 3461.

(12) Hutter, E. M.; Gélvez-Rueda, M. C.; Osherov, A.; Bulović, V.; Grozema, F. C.; Stranks, S. D.; Savenije, T. J. Direct−Indirect Character of the Bandgap in Methylammonium Lead Iodide Perovskite. *Nat. Mater.* **2017**, *16*, 115−120.

(13) Crothers, T. W.; Milot, R. L.; Patel, J. B.; Parrott, E. S.; Schlipf, J.; Müller-Buschbaum, P.; Johnston, M. B.; Herz, L. M. Photon Reabsorption Masks Intrinsic Bimolecular Charge-Carrier Recombination in $CH_3NH_3PbI_3$ Perovskite. *Nano Lett.* **2017**, *17*, 5782−5789.

(14) Fabini, D. H.; Laurita, G.; Bechtel, J. S.; Stoumpos, C. C.; Evans, H. A.; Kontos, A. G.; Raptis, Y. S.; Falaras, P.; Van der Ven, A.; Kanatzidis, M. G.; et al. Dynamic Stereochemical Activity of the Sn^{2+} Lone Pair in Perovskite $CsSnBr_3$. *J. Am. Chem. Soc.* **2016**, *138*, 11820−11832.

(15) Fu, Y.; Jin, S.; Zhu, X.-Y. Stereochemical Expression of ns^2 Electron Pairs in Metal Halide Perovskites. *Nat. Rev. Chem* **2021**, *5*, 838−852.

(16) Adams, D. J.; Churakov, S. V. Classification of Perovskite Structural Types with Dynamical Octahedral Tilting. *IUCrJ* **2023**, *10*, 309−320.

(17) Cannelli, O.; Wiktor, J.; Colonna, N.; Leroy, L.; Puppin, M.; Bacellar, C.; Sadykov, I.; Krieg, F.; Smolentsev, G.; Kovalenko, M. V.; et al. Atomic-Level Description of Thermal Fluctuations in Inorganic Lead Halide Perovskites. *J. Phys. Chem. Lett.* **2022**, *13*, 3382−3391.

(18) Beecher, A. N.; Semonin, O. E.; Skelton, J. M.; Frost, J. M.; Terban, M. W.; Zhai, H.; Alatas, A.; Owen, J. S.; Walsh, A.; Billinge, S. J. Direct Observation of Dynamic Symmetry Breaking Above Room Temperature in Methylammonium Lead Iodide Perovskite. *ACS Energy Lett.* **2016**, *1*, 880−887.

(19) Page, K.; Siewenie, J. E.; Quadrelli, P.; Malavasi, L. Short-Range Order of Methylammonium and Persistence of Distortion at the Local Scale in $MAPbBr_3$ Hybrid Perovskite. *Angew. Chem.* **2016**, *128*, 14532−14536.

(20) Bernasconi, A.; Page, K.; Dai, Z.; Tan, L. Z.; Rappe, A. M.; Malavasi, L. Ubiquitous Short-Range Distortion of Hybrid Perovskites and Hydrogen-Bonding Role: The $MAPbCl_3$ Case. *J. Phys. Chem. C* **2018**, *122*, 28265−28272.

(21) Morana, M.; Wiktor, J.; Coduri, M.; Chiara, R.; Giacobbe, C.; Bright, E. L.; Ambrosio, F.; De Angelis, F.; Malavasi, L. Cubic or Not Cubic? Combined Experimental and Computational Investigation of the Short-Range Order of Tin Halide Perovskites. *J. Phys. Chem. Lett.* **2023**, *14*, 2178−2186.

(22) Wiktor, J.; Rothlisberger, U.; Pasquarello, A. Predictive Determination of Band Gaps of Inorganic Halide Perovskites. *J. Phys. Chem. Lett.* **2017**, *8*, 5507−5512.

(23) Zhao, X.-G.; Dalpian, G. M.; Wang, Z.; Zunger, A. Polymorphous Nature of Cubic Halide Perovskites. *Phys. Rev. B* **2020**, *101*, 155137.

(24) Wang, H.; Tal, A.; Bischoff, T.; Gono, P.; Pasquarello, A. Accurate and Efficient Band-Gap Predictions for Metal Halide Perovskites at Finite Temperature. *npj Comput. Mater.* **2022**, *8*, 237.

(25) Yang, R. X.; Skelton, J. M.; Da Silva, E. L.; Frost, J. M.; Walsh, A. Spontaneous Octahedral Tilting in the Cubic Inorganic Cesium Halide Perovskites $CsSnX_3$ and $CsPbX_3$ (X=F, Cl, Br, I). *J. Phys. Chem. Lett.* **2017**, *8*, 4720−4726.

(26) Yang, R. X.; Skelton, J. M.; Da Silva, E. L.; Frost, J. M.; Walsh, A. Assessment of Dynamic Structural Instabilities Across 24 Cubic Inorganic Halide Perovskites. *J. Chem. Phys.* **2020**, *152*, 024703.

(27) Kaczkowski, J.; Płowaś-Korus, I. The Vibrational and Thermodynamic Properties of $CsPbI_3$ Polymorphs: An Improved Description Based on the SCAN Meta-GGa Functional. *J. Phys. Chem. Lett.* **2021**, *12*, 6613−6621.

(28) Kaiser, W.; Carignano, M.; Alothman, A. A.; Mosconi, E.; Kachmar, A.; Goddard, W. A., III; De Angelis, F. First-Principles Molecular Dynamics in Metal-Halide Perovskites: Contrasting Generalized Gradient Approximation and Hybrid Functionals. *J. Phys. Chem. Lett.* **2021**, *12*, 11886−11893.

(29) Fransson, E.; Wiktor, J.; Erhart, P. Phase Transitions in Inorganic Halide Perovskites from Machine-Learned Potentials. *J. Phys. Chem. C* **2023**, *127*, 13773−13781.

(30) Ghosh, D.; Atkins, P. W.; Islam, M. S.; Walker, A. B.; Eames, C. Good Vibrations: Locking of Octahedral Tilting in Mixed-Cation Iodide Perovskites for Solar Cells. *ACS Energy Lett.* **2017**, *2*, 2424−2429.

(31) Fransson, E.; Rosander, P.; Eriksson, F.; Rahm, J. M.; Tadano, T.; Erhart, P. Limits of the Phonon Quasi-Particle Picture at the Cubic-To-Tetragonal Phase Transition in Halide Perovskites. *Commun. Phys.* **2023**, *6*, 173.

(32) Carignano, M. A.; Aravindh, S. A.; Roqan, I. S.; Even, J.; Katan, C. Critical Fluctuations and Anharmonicity in Lead Iodide Perov-

https://doi.org/10.1021/acs.chemmater.3c00933
Chem. Mater. 2023, 35, 6737−6744

skites from Molecular Dynamics Supercell Simulations. *J. Phys. Chem. C* **2017**, *121*, 20729−20738.
(33) Fan, Z.; Zeng, Z.; Zhang, C.; Wang, Y.; Song, K.; Dong, H.; Chen, Y.; Ala-Nissila, T. Neuroevolution Machine Learning Potentials: Combining High Accuracy and Low Cost in Atomistic Simulations and Application to Heat Transport. *Phys. Rev. B* **2021**, *104*, 104309.
(34) Fan, Z.; Wang, Y.; Ying, P.; Song, K.; Wang, J.; Wang, Y.; Zeng, Z.; Xu, K.; Lindgren, E.; Rahm, J. M.; et al. GPUMD: A Package for Constructing Accurate Machine-Learned Potentials and Performing Highly Efficient Atomistic Simulations. *J. Chem. Phys.* **2022**, *157*, 114801.
(35) calorine, 2022. https://gitlab.com/materials-modeling/calorine, (accessed Feb 21, 2023).
(36) Eriksson, F.; Fransson, E.; Erhart, P. The Hiphive Package for the Extraction of High-Order Force Constants by Machine Learning. *Adv. Theory Simul.* **2019**, *2*, 1800184.
(37) Blöchl, P. E. Projector Augmented-Wave Method. *Phys. Rev. B: Condens. Matter Mater. Phys.* **1994**, *50*, 17953−17979.
(38) Kresse, G.; Joubert, D. From Ultrasoft Pseudopotentials to the Projector Augmented-Wave Method. *Phys. Rev. B: Condens. Matter Mater. Phys.* **1999**, *59*, 1758−1775.
(39) Kresse, G.; Hafner, J. Ab Initio Molecular Dynamics for Liquid Metals. *Phys. Rev. B: Condens. Matter Mater. Phys.* **1993**, *47*, 558−561.
(40) Kresse, G.; Furthmüller, J. Efficiency of Ab-Initio Total Energy Calculations for Metals and Semiconductors Using a Plane-Wave Basis Set. *Comput. Mater. Sci.* **1996**, *6*, 15−50.
(41) Perdew, J. P.; Burke, K.; Ernzerhof, M. Generalized Gradient Approximation Made Simple. *Phys. Rev. Lett.* **1996**, *77*, 3865−3868.
(42) Perdew, J. P.; Ruzsinszky, A.; Csonka, G. I.; Vydrov, O. A.; Scuseria, G. E.; Constantin, L. A.; Zhou, X.; Burke, K. Restoring the Density-Gradient Expansion for Exchange in Solids and Surfaces. *Phys. Rev. Lett.* **2008**, *100*, 136406.
(43) Sun, J.; Ruzsinszky, A.; Perdew, J. P. Strongly Constrained and Appropriately Normed Semilocal Density Functional. *Phys. Rev. Lett.* **2015**, *115*, 036402.
(44) Peng, H.; Yang, Z.-H.; Perdew, J. P.; Sun, J. Versatile Van Der Waals Density Functional Based on a Meta-Generalized Gradient Approximation. *Phys. Rev. X* **2016**, *6*, 041005.
(45) Dion, M.; Rydberg, H.; Schröder, E.; Langreth, D. C.; Lundqvist, B. I. Van Der Waals Density Functional for General Geometries. *Phys. Rev. Lett.* **2004**, *92*, 246401.
(46) Berland, K.; Hyldgaard, P. Exchange Functional That Tests the Robustness of the Plasmon Description of the Van Der Waals Density Functional. *Phys. Rev. B: Condens. Matter Mater. Phys.* **2014**, *89*, 035412.
(47) Fan, Z.; Pereira, L. F. C.; Wang, H.-Q.; Zheng, J.-C.; Donadio, D.; Harju, A. Force and Heat Current Formulas for Many-Body Potentials in Molecular Dynamics Simulations with Applications to Thermal Conductivity Calculations. *Phys. Rev. B: Condens. Matter Mater. Phys.* **2015**, *92*, 094301.
(48) Bussi, G.; Donadio, D.; Parrinello, M. Canonical Sampling Through Velocity Rescaling. *J. Chem. Phys.* **2007**, *126*, 014101.
(49) Bussi, G.; Donadio, D. Canonical Sampling Through Velocity Rescaling. *J. Chem. Phys.* **2007**, *126*, 014101.
(50) Stukowski, A. Visualization and Analysis of Atomistic Simulation Data with OVITO−the Open Visualization Tool. *Modell. Simul. Mater. Sci. Eng.* **2009**, *18*, 015012.
(51) Larsen, P. M.; Schmidt, S.; Schiøtz, J. Robust Structural Identification Via Polyhedral Template Matching. *Modell. Simul. Mater. Sci. Eng.* **2016**, *24*, 055007.
(52) Virtanen, P.; Gommers, R.; Oliphant, T. E.; Haberland, M.; Reddy, T.; Cournapeau, D.; Burovski, E.; Peterson, P.; Weckesser, W.; Bright, J.; et al. SciPy 1.0: Fundamental Algorithms for Scientific Computing in Python. *Nat. Methods* **2020**, *17*, 261−272.
(53) Marronnier, A.; Roma, G.; Boyer-Richard, S.; Pedesseau, L.; Jancu, J.-M.; Bonnassieux, Y.; Katan, C.; Stoumpos, C. C.; Kanatzidis, M. G.; Even, J. Anharmonicity and Disorder in the Black Phases of Cesium Lead Iodide Used for Stable Inorganic Perovskite Solar Cells. *ACS Nano* **2018**, *12*, 3477−3486.
(54) Bokdam, M.; Lahnsteiner, J.; Ramberger, B.; Schäfer, T.; Kresse, G. Assessing Density Functionals Using Many Body Theory for Hybrid Perovskites. *Phys. Rev. Lett.* **2017**, *119*, 145501.
(55) Doherty, T. A.; Nagane, S.; Kubicki, D. J.; Jung, Y.-K.; Johnstone, D. N.; Iqbal, A. N.; Guo, D.; Frohna, K.; Danaie, M.; Tennyson, E. M.; et al. Stabilized Tilted-Octahedra Halide Perovskites Inhibit Local Formation of Performance-Limiting Phases. *Science* **2021**, *374*, 1598−1605.
(56) Lanigan-Atkins, T.; He, X.; Krogstad, M.; Pajerowski, D.; Abernathy, D.; Xu, G. N.; Xu, Z.; Chung, D.-Y.; Kanatzidis, M.; Rosenkranz, S.; et al. Two-Dimensional Overdamped Fluctuations of the Soft Perovskite Lattice in $CsPbBr_3$. *Nat. Mater.* **2021**, *20*, 977−983.
(57) Weadock, N. J.; Sterling, T. C.; Vigil, J. A.; Gold-Parker, A.; Smith, I. C.; Ahammed, B.; Krogstad, M. J.; Ye, F.; Voneshen, D.; Gehring, P. M.; et al. The Nature of Dynamic Local Order in $CH_3NH_3PbI_3$ and $CH_3NH_3PbBr_3$. *Joule* **2023**, *7*, 1051−1066.
(58) Baldwin, W.; Liang, X.; Klarbring, J.; Dubajic, M.; Dell'Angelo, D.; Sutton, C.; Caddeo, C.; Stranks, S. D.; Mattoni, A.; Walsh, A., et al. Dynamic Local Structure in Caesium Lead Iodide: Spatial Correlation and Transient Domains. arXiv 2023, Condensed Matter, Materials Science, April 11, 2023, Ver. 2. https://arxiv.org/abs/2304.04714 (accessed Aug 7, 2023).

https://doi.org/10.1021/acs.chemmater.3c00933
Chem. Mater. 2023, 35, 6737−6744

Supplemental Material:

Quantifying Dynamic Tilting in Halide Perovskites: Chemical Trends and Local Correlations

Julia Wiktor[1,*], Erik Fransson[1], Dominik Kubicki[2], and Paul Erhart[1,*]

[1] *Department of Physics, Chalmers University of Technology, SE-41296, Gothenburg, Sweden*
[2] *School of Chemistry, University of Birmingham, Birmingham, UK*
[*] *julia.wiktor@chalmers.se, erhart@chalmers.se*

Contents

Supplemental Figures

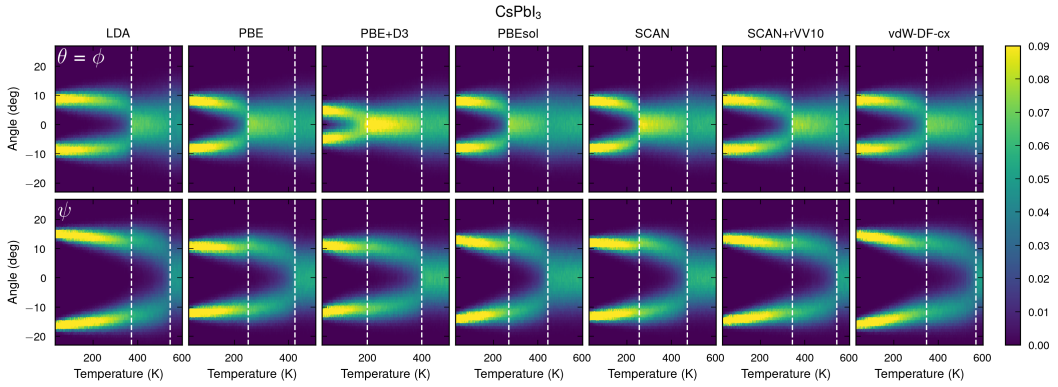

Figure S1: Maps of tilt angles as a function of temperature $CsPbI_3$ from models based on all seven functional. Dashed vertical lines indicate the orthorhombic-to-tetragonal and tetragonal-to-cubic phase transitions.

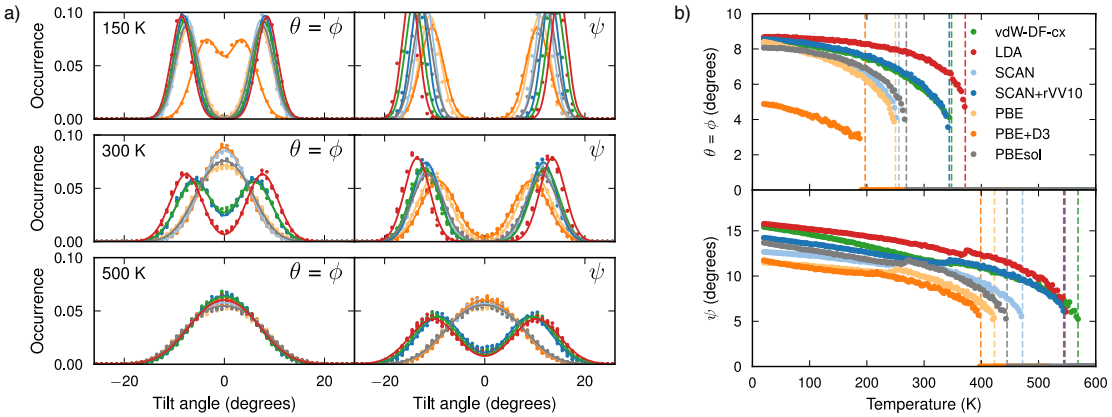

Figure S2: (a) Probability distribution of octahedral tilts at 150, 300, and 500 K in $CsPbI_3$ calculated using all considered functionals, as described by the three Euler angles θ, ϕ, and ψ. (b) Position of the maximum in the tilt angle distribution as extracted from double Gaussian fits. Vertical dashed lines indicate phase transitions.

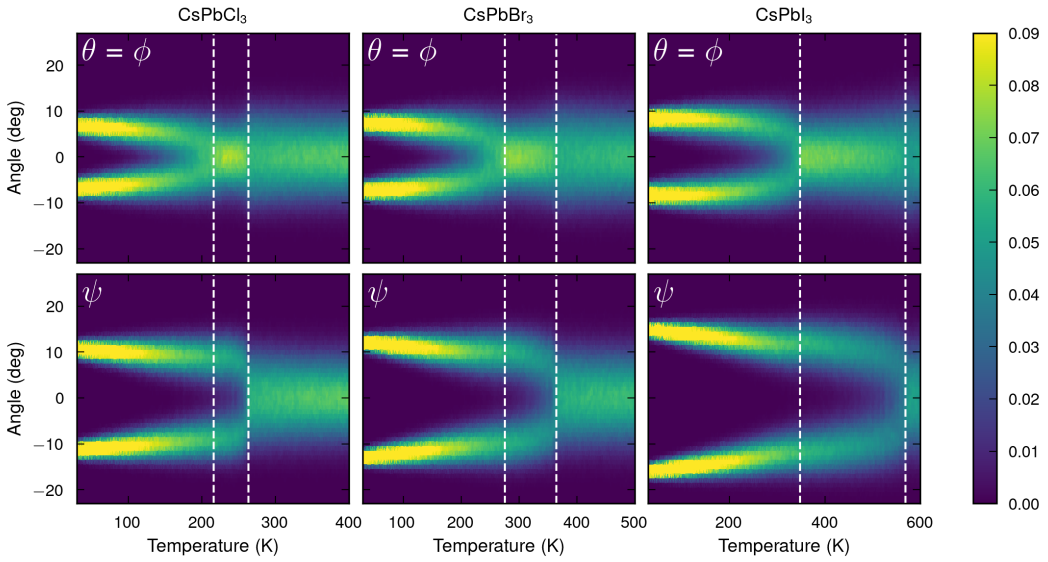

Figure S3: Maps of tilt angles as a function of temperature in $CsPbCl_3$, $CsPbBr_3$, and $CsPbI_3$ from models based on the vdW-DF-cx functional. Dashed vertical lines indicate the orthorhombic-to-tetragonal and tetragonal-to-cubic phase transitions.

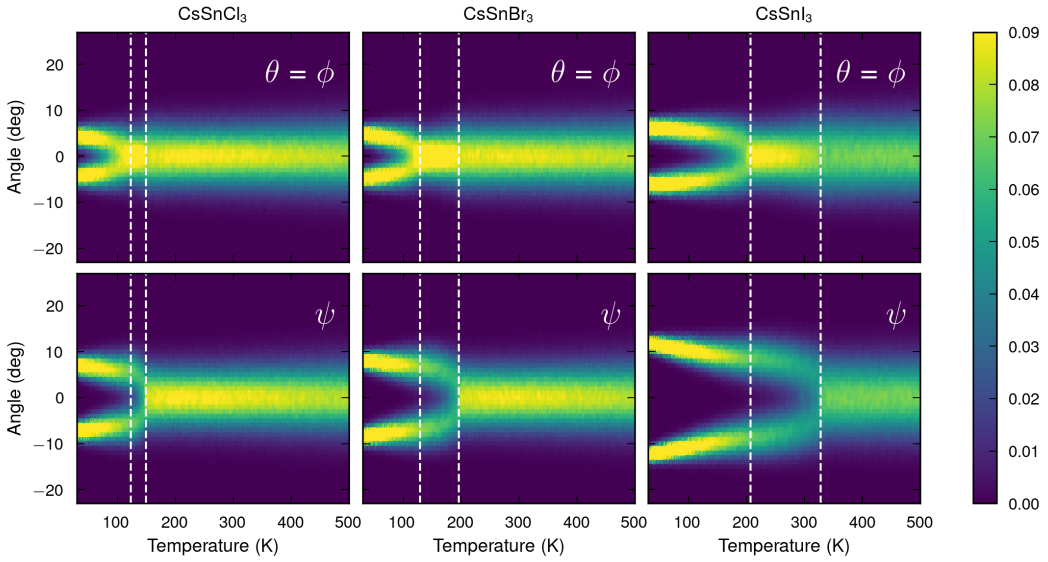

Figure S4: Maps of tilt angles as a function of temperature in $CsSnCl_3$, $CsSnBr_3$, and $CsSnI_3$ from models based on the vdW-DF-cx functional. Dashed vertical lines indicate the orthorhombic-to-tetragonal and tetragonal-to-cubic phase transitions.

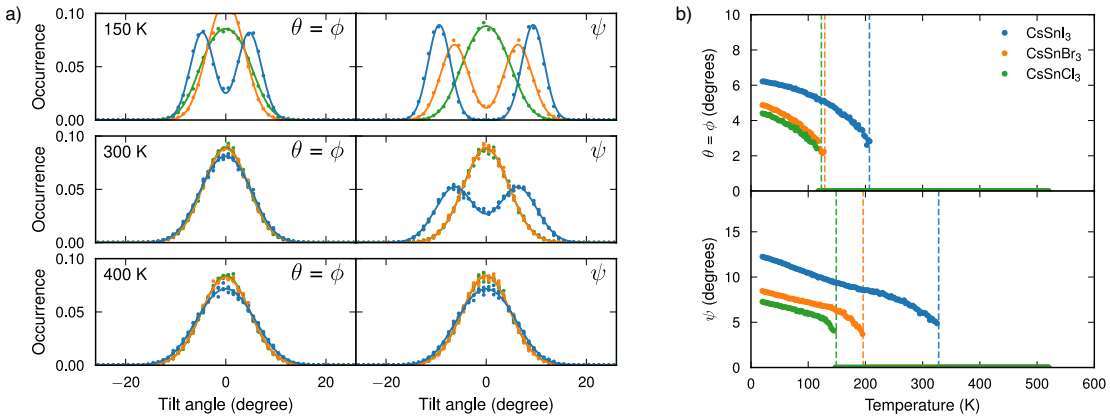

Figure S5: (a) Probability distribution of octahedral tilts at 150, 300, and 400 K in $CsSnCl_3$, $CsSnBr_3$, and $CsSnI_3$, as described by the three Euler angles θ, ϕ, and ψ. (b) Position of the maximum in the tilt angle distribution as extracted from double Gaussian fits. Vertical dashed lines indicate phase transitions.

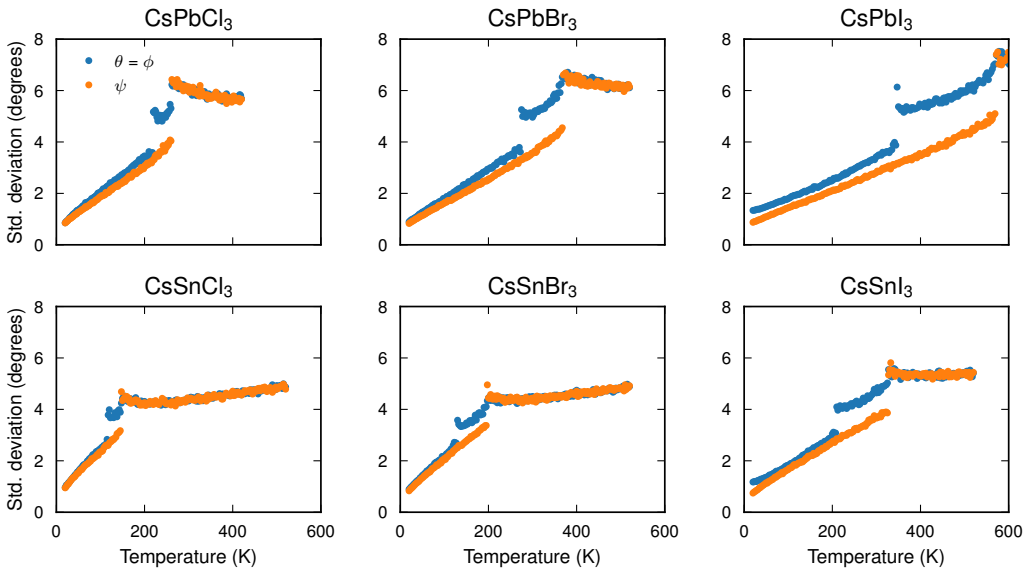

Figure S6: Standard deviation σ of the tilt angle distributions as extracted from double Gaussian fits.

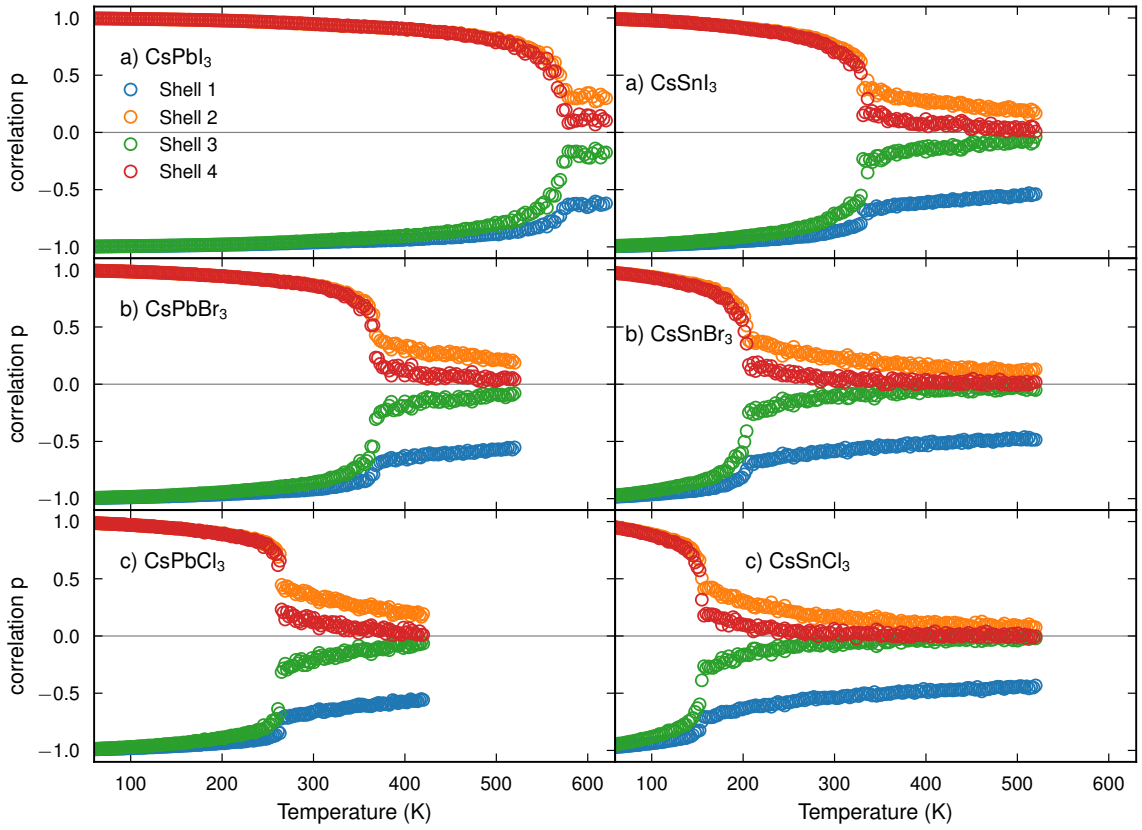

Figure S7: The correlation p of tilt-angles around the z-axis calculated along heating simulation for the neighbor shells along the [100] direction.

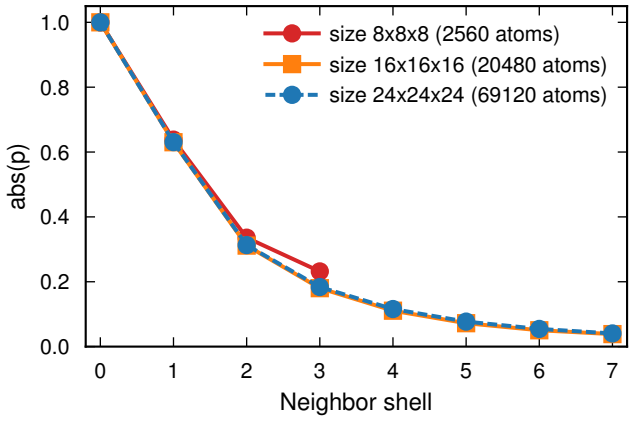

Figure S8: The absolute value of the correlation, $|p|$, of tilt-angles around the z-axis calculated for $CsPbI_3$ for constant temperature MD simulations at T=600 K for various system sizes.

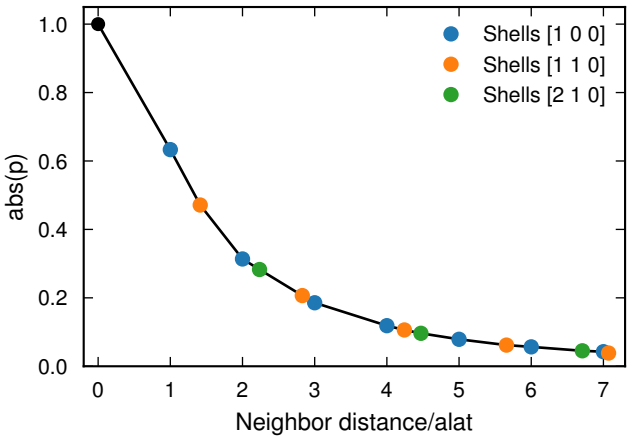

Figure S9: The absolute value of the correlation, $|p|$, of tilt-angles around the z-axis calculated for $CsPbI_3$ for constant temperature MD simulations at T=600 K for various neighbor shell directions.

Supplemental Tables

Table S1: Overview of data used for training NEP models. $N_{\text{structures}}$: Number of structures. N_{atoms}: Total number of atoms. R^2: coefficient of determination. RMSE: root mean squared error in units of meV atom^{-1}, meV Å^{-1}, and meV atom^{-1} for energy, forces, and virials, respectively.

Material	XC	$N_{\text{structures}}$	N_{atoms}	Energy		Forces		Virials	
				R^2	RMSE	R^2	RMSE	R^2	RMSE
$CsPbCl_3$	vdW-DF-cx	633	65 820	0.99994	0.7	0.98745	48.1	0.99975	9.7
$CsPbBr_3$	vdW-DF-cx	618	63 255	0.99996	0.6	0.98623	46.0	0.99981	8.5
$CsPbI_3$	vdW-DF-cx	674	65 060	0.99984	1.2	0.98532	49.1	0.99965	11.6
$CsPbI_3$	LDA	674	65 060	0.99982	0.9	0.98331	47.6	0.99962	10.8
$CsPbI_3$	PBE	510	45 800	0.99995	0.7	0.98579	43.7	0.99977	9.6
$CsPbI_3$	PBE+D3	509	45 780	0.99992	0.8	0.98537	44.4	0.99975	9.4
$CsPbI_3$	PBEsol	697	69 340	0.99990	1.2	0.99071	51.3	0.99972	12.0
$CsPbI_3$	SCAN	658	61 380	0.99987	1.6	0.98656	52.5	0.99971	13.9
$CsPbI_3$	SCAN+rVV10	658	61 380	0.99986	1.5	0.98678	52.3	0.99972	13.3
$CsSnCl_3$	vdW-DF-cx	751	72 085	0.99988	1.0	0.98188	61.8	0.99951	13.3
$CsSnBr_3$	vdW-DF-cx	785	77 500	0.99992	0.9	0.98214	56.5	0.99952	13.8
$CsSnI_3$	vdW-DF-cx	778	77 420	0.99979	1.5	0.97910	56.9	0.99957	13.3

Table S2: Atomic shells treated among the valence electrons in the projector augmented wave setups used in the VASP DFT calculations.

Element	Valence configuration
Cs	$5s^2 5p^6 6s^1$
Sn	$5s^2 5p^2$
Pb	$6s^2 6p^2$
Cl	$3s^2 3p^5$
Br	$4s^2 4p^5$
I	$5s^2 5p^5$

Table S3: Phase transition temperatures in K found for different halide perovskites using the vdW-DF-cx functional. Values were extracted from the temperature dependence of heat capacity.

	ortho-tetra	tetra-cubic
$CsPbCl_3$	216	263
$CsPbBr_3$	276	365
$CsPbI_3$	348	569
$CsSnCl_3$	123	149
$CsSnBr_3$	129	196
$CsSnI_3$	207	328